applied optics

Method for improving the positional accuracy in passive optical detection of space objects

Ranga Rosok,[1,*] Nils Bartels,[1] Wolfgang Riede,[1] Moritz Vogel,[1] Paul Wagner,[2] and Thomas Dekorsy[1]

[1]Institute of Technical Physics, German Aerospace Center (DLR), Stuttgart, Germany
[2]Institute of Communications and Navigation, German Aerospace Center (DLR), Oberpfaffenhofen-Wessling, Germany
*ranga.rosok@dlr.de

Received 10 April 2024; revised 22 May 2024; accepted 23 May 2024; posted 24 May 2024; published 17 June 2024

The number of space objects, i.e., active satellites as well as space debris, is growing at an exponential rate. The management of congested space requires networks of sensors to detect and precisely measure the positions of objects in space. We describe a method that improves the positional accuracy of passive optical detection of space objects. The method is based on a laboratory sensor calibration, which is suitable for all types of cameras (CCD and CMOS cameras) and can easily be implemented for existing staring or tracking stations or even used with space-based passive optical sensors. The successful implementation of the method is demonstrated in a test campaign by measuring tracklets of several Earth-orbiting satellites with a ground-based staring system known as APPARILLO. In addition to its use in space object detection, we encourage that the presented method might also inspire other fields of research and technology, where images need to be acquired with precise timing.

https://doi.org/10.1364/AO.526011

1. INTRODUCTION

Modern space traffic management (STM) requires networks of sensors that constantly detect and determine the positions and orbits of objects in space [1,2]. While space object detection has traditionally been a domain of the military, the commercialization of space has also driven the development of a growing STM market. STM companies build catalogues of space objects and offer services such as providing positional data of satellites, risk analysis of collisions with space debris, and even real-time collision warnings between space objects to customers such as satellite operators, space agencies, and insurance companies [3].

In the latest Space Strategy of the German government, space, particularly low-Earth orbit (LEO), was declared as critical infrastructure requiring preservation. Among its 13 key projects, the strategy outlines the development and expansion of national space situational awareness capabilities as one priority. Another key initiative involves the establishment of a STM system in collaboration with the European Union, with a specific emphasis on enhancing independence in terms of staring and tracking capabilities [4].

The detection of space objects is mostly performed either via active radio detection and ranging (RADAR) stations or via the passive optical detection of sunlight reflected from space objects. Examples of modern STM RADAR stations include the US AN/FSY Space Fence RADAR [5] or the network of phased-array RADARs of the company Leolabs Inc. [6], and they have the major advantage of being able to operate under all weather conditions.

Since passive optical sensors use the sun as a naturally occurring source of electromagnetic waves, they—compared to RADAR systems—offer the advantage of consuming less energy, being typically a lot cheaper, and detecting objects at great distances (geostationary orbits and beyond) not covered by RADAR. Although companies have started building networks of space based optical sensors [7], most passive optical sensors for STM are placed on Earth. Examples of networks of passive optical sensors include the SmartNETTM sensor network [8] and a commercial network run by Slingshot Aerospace. Additional driving forces for building optical sensors are the opportunity of combining passive optical and laser ranging measurements for high-precision orbit determinations [9,10], as well as the opportunity of measuring optical light curves (time-dependent intensity variations detected by the optical sensor), which can be analyzed to obtain additional information on space objects such as the rotational motion or the material composition [11–13].

A challenge of obtaining a high positional accuracy with passive optical sensors is that although scientific cameras take or provide a trigger signal indicating the start/stop of the image exposure (typically converted to a timestamp via a GPS timer), the exposures of different pixels for most cameras do not start

and stop at the exact same time. Cameras without this timing issue use a detection mode known as "true global shutter" but are not yet as readily available as large-scale astronomy grade cameras and have other disadvantages such as increased price, power consumption, and noise level [14]. We would like to note that there are many cameras featuring a detection mode known as "rolling shutter with global reset" [14], which would also require a timing calibration, but are often marketed as a camera with a "global shutter."

A first approach to introduce a pixel dependent timing correction in space object detection has very recently been proposed by the company Sybilla Technologies [15]. In that work, the authors used an optical sensor with a "rolling shutter" and managed to retrieve information on the line period that was then used as a pixel-dependent timing correction, as an addition to a fixed timing offset that was determined via the detection of satellites with well-known ephemerides.

The presented work advances beyond previous efforts by introducing a novel method that directly measures an absolute, pixel-dependent time bias. This bias accounts for the delay between a trigger signal and the start/end of image acquisition in a straightforward laboratory setup. This method is versatile, applicable to all types of cameras (CCD and CMOS) and electronic (e.g., rolling shutters) or mechanical shutters (e.g., blade shutters). It is also not limited to sensors operating in the visible but could also be used with short-wave infrared (SWIR) sensors that have been proposed for daylight tracking of space debris [16] and remove the need for a calibration campaign on satellites with well-known orbits to measure the time bias.

We demonstrate the success of the method by its implementation into a fully autonomous passive optical staring system known as APPARILLO [17]. Via a validation campaign in which we detect tracklets of several satellites in low-Earth orbits (LEO), we find that the along track error (in direction of flight) is reduced by a factor of 5.8 compared to measurements without this pixel-dependent timing correction.

2. CONCEPT

Figure 1 shows an example of a satellite streak from a satellite in LEO as detected with a passive optical staring sensor (pointing to a fixed direction in the sky) with an exposure time of 1 s. The celestial angular coordinates of the starting and ending points of the streak can be determined with an astrometric calibration (localization among fixed stars in the vicinity of the satellite) and combined with the associated timestamps t_0 and t_1.

For tracking a telescope object, the tracked space object will form a point in the image, and the stars instead form streaks that need to be further analyzed. In both cases, the outcome of passive optical detections of space objects primarily consist of two angular coordinates, φ_{Ra} and φ_{Dec}, accompanied by a corresponding timestamp, t. This information (together with system data gathered in a header) is then typically used to generate a tracking data message (TMD) [18], which can be used as an input for the calculation of orbital data of the space object. Thus, the positional accuracy of detected space objects primarily determined by these three values,

$$\boldsymbol{P} = \{t, \varphi_{\mathrm{Ra}}, \varphi_{\mathrm{Dec}}\}, \tag{1}$$

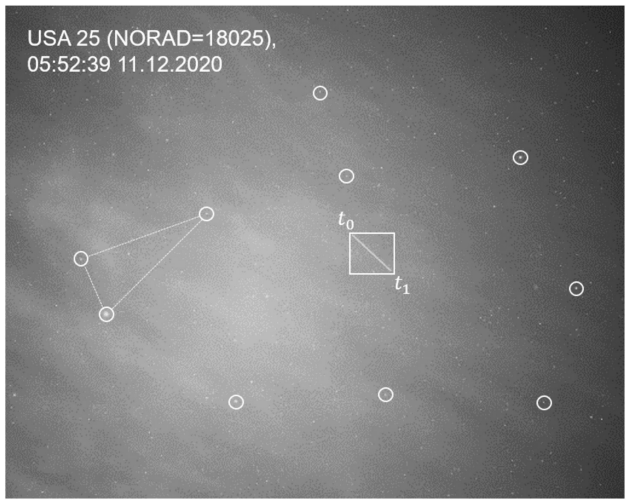

Fig. 1. Annotated example image of a satellite streak produced by sunlit LEO satellite USA 25 (NORAD ID 18025), captured using a passive optical staring system directed towards a fixed position in the sky.

has a direct influence of the achievable orbit accuracy and thus also on other import derived data, such as the collision risk with other space objects, which is important for making decisions, such as initializing collision avoidance maneuvers. For a more in-depth analysis and potential improvement of accuracy, the associated error can be categorized into two distinct groups. The first category is position-related and is directly linked to the two angular coordinates φ_{Ra} and φ_{Dec}. Various factors contribute to this category, including the precision of astrometric calibration, which, in turn, is influenced by the accuracy of the star catalog, the detection algorithm of the stars, and the interpolation of the object's location to the nearest stars.

The accuracy of the detection algorithm for the object itself also significantly influences this category. In instances where the object is recorded as a streak, determining the correct starting and ending points of the streak, involving the determination of the line width to identify the endpoints, is crucial. Additionally, this algorithm must exhibit robustness against noise and stars in proximity to the streak to ensure accurate automatic detection.

The second crucial factor influencing positional accuracy is the correct timing of the image. The timestamp t associates φ_{Ra} and φ_{Dec} with the correct position in time. Any error in t directly translates to an error in the object's position, considering that the object moves at a certain speed. To mitigate this error, the timestamp t needs to be as accurate as possible. Commonly, a GPS timer connected to the camera is used to achieve precise time synchronization of the exposure start and stop times with UTC time.

This paper will concentrate on enhancing the timing accuracy beyond the limits set by GPS timers. Additionally it will refine the astrometric calibration beyond the utilized standard method to further evaluate the performance of the timing correction.

For cameras without a "true global shutter," the exposure (start and stop) time of individual pixels varies depending on their position in the image. For example, mechanical blade shutters (opening from the center towards the outside) can exhibit

timing differences on the order of multiple tens of microseconds between the center-pixel and pixels located on the outside [19]. Electronic rolling shutters have timing differences between the first and last pixel of the image, which are on the same order of magnitude [20].

The proposed method aims to compensate for these individual timing differences via a laboratory calibration, with the goal of achieving a timing accuracy comparable to that of global shutter cameras. Both global shutter and non-global shutter cameras may exhibit a constant timing offset across the entire image, arising from a delay between the actual exposure start and the trigger signal used for GPS synchronization. The presented method will also compensate for this constant offset.

Prior to diving into the details of the proposed method, the subsequent discussion provides a brief overview of how the error resulting from timing discrepancies can be assessed.

As discussed earlier, the position of an object in the equatorial, celestial coordinate system can be expressed by two angular coordinates, φ_{Ra} and φ_{Dec}, along with a timestamp t. We define an angular error $\boldsymbol{\Delta\varphi}$ as the difference between the actual position and the measured position of the object at time t, resulting in a set of angular coordinates $\Delta\varphi_{\mathrm{Ra}}$ and $\Delta\varphi_{\mathrm{Dec}}$,

$$\boldsymbol{\Delta\varphi} = \boldsymbol{\varphi}_{\mathrm{measured}} - \boldsymbol{\varphi}_{\mathrm{actual}}. \tag{2}$$

A coordinate transformation to a satellite-related coordinate system is employed to provide more insight into the error values. This paper refers to the along track, cross track, and radial system with the following definitions:

The radial axis $\hat{\boldsymbol{e}}_r$ is pointing from the center of the Earth towards the position $\boldsymbol{r}$ of the satellite,

$$\hat{\boldsymbol{e}}_r = \frac{\boldsymbol{r}}{|\boldsymbol{r}|}. \tag{3}$$

The cross track axis $\hat{\boldsymbol{e}}_c$ is orthogonal to the radial axis and the current velocity vector $\boldsymbol{v}$ of the satellite,

$$\hat{\boldsymbol{e}}_{\mathrm{c}} = \frac{\boldsymbol{v} \times \hat{\boldsymbol{e}}_r}{|\boldsymbol{v} \times \hat{\boldsymbol{e}}_r|}. \tag{4}$$

The along track axis $\hat{\boldsymbol{e}}_a$ is orthogonal to the radial and cross track axis,

$$\hat{\boldsymbol{e}}_a = \hat{\boldsymbol{e}}_r \times \hat{\boldsymbol{e}}_c. \tag{5}$$

For small time periods the satellite moves approximately only in the direction of the along track axis, meaning that after a small time period of Δt only the along track coordinate has changed. This approximation can be reversed, an error in time Δt would (mostly) contribute to the along track error Δa, which is defined as the projection of the absolute error vector $\boldsymbol{\Delta} r$ onto the along track axis $\hat{\boldsymbol{e}}_a$,

$$\Delta a = \boldsymbol{\Delta} r \cdot \hat{\boldsymbol{e}}_a. \tag{6}$$

The ratio between the along track error Δa and the cross track error Δc provides a metric η that describes the dominance of the along track error and can be used as an indicator for the accuracy of the timing,

$$\eta = \frac{|\Delta a|}{|\Delta c|}. \tag{7}$$

In the absence of timing errors, the ratio scatters around 1 since positional errors contribute equally to the along and cross track error. In the presence of timing errors (e.g., due to different, uncorrected read-out times for different pixels), the mean ratio will be greater than 1 since the along track error is greater than the cross track error.

In the following, we'll outline the proposed method for improving the positional accuracy in the detection of space objects. Following the state of the art, staring images are recorded. The starting and ending coordinates of streaks (e.g., arising from illuminated space objects in LEO) are determined with a streak detection algorithm. While there are also advanced algorithms for the detection of faint space objects [15,21,22], this work uses a classical streak detection algorithm [23], which has been shown to perform extremely well under adverse conditions, such as partial cloud coverage. These are the two sets of coordinates $\boldsymbol{P}_i$, one at the starting time t_1 and the end time t_2 of each detected streak:

$$\boldsymbol{P}_i = \{t_i, x_i, y_i\}, \quad i = 1, 2, \tag{8}$$

where x_i, y_i are the coordinates of the streak in the image. These coordinates can then be converted to celestial coordinates using an astrometric analysis.

To determine which of the two points in the streak is the starting point $\boldsymbol{P}_1$ and which is the end-point $\boldsymbol{P}_2$, two images with the same detected object at two different times are used. The center of the streak $\boldsymbol{P}_{ij}$ is calculated by averaging the two points of one image,

$$\boldsymbol{P}_{ij} = \frac{1}{2}\left(\boldsymbol{P}_i + \boldsymbol{P}_j\right), \tag{9}$$

and is associated with an average time t_{ij}.

The difference between the mean positions ΔP of two images is now exactly defined as

$$\boldsymbol{\Delta} P = \boldsymbol{P}_{kl} - \boldsymbol{P}_{ij}; \quad \Delta t = t_{kl} - t_{ij} > 0, \tag{10}$$

and it points into the direction of the movement of the satellite. This information can be used to determine which two points in the first image, as well as the second image, are the starting and ending points. This algorithm is depicted in Fig. 2.

The time correction algorithm alters the time stamp t_i of each point $\boldsymbol{P}_i$ by adding an individual delay $dt(c, x_i, y_i) \in \mathbb{R}$ to each point,

$$\boldsymbol{P}_i = \{t_i + dt(c, x_i, y_i), x_i, y_i\}. \tag{11}$$

This delay time is dependent on the individual pixel coordinates (x_i, y_i), is measured in with a laboratory calibration (as will be described in the following section), and is stored in an array or a function that maps this relationship.

In general, the delay time dt is also influenced by the classification c of the streak point, distinguishing between a starting or stopping point. Thus, there are in general two timing arrays, one for the starting points of each streak and one for the stopping points.

The impact of shutter time correction primarily depends on two factors, the angular movement speed $\dot{\varphi}$ of the target relative to the observer and the value of the delay array dt at the

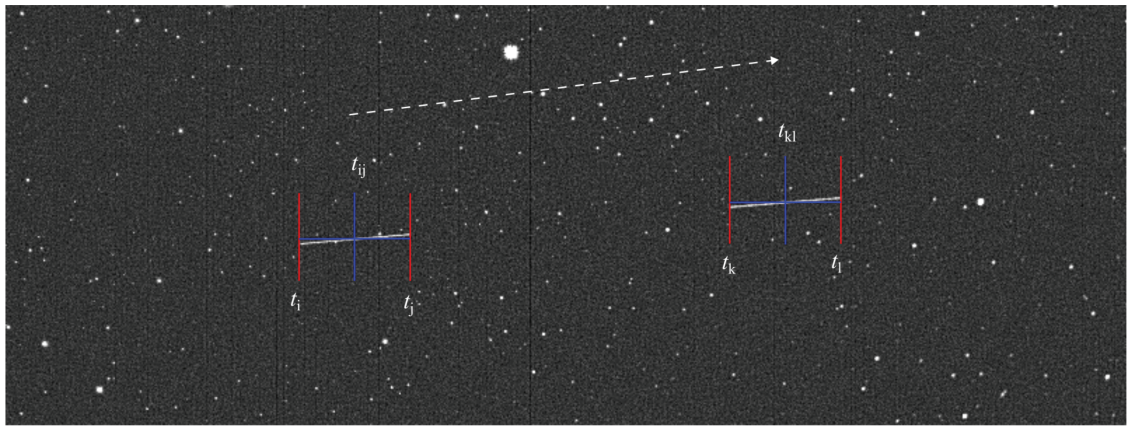

Fig. 2. Cutout of two merged images showing a detected streak. Initially, the correlation between time stamps $t_{i,j,k,l}$ is unknown. By comparing the mean position and timestamp t_{ij} with t_{kl} obtained from the second image, the flight direction is determined, enabling the identification of the streak's starting and ending points.

recorded position. This relationship can be explained through the following fundamental formula:

$$\Delta a = \dot{\varphi} \cdot dt, \tag{12}$$

where Δa represents the angular error. Notably, this formula indicates that a correction of Δa is not affected by other factors such as the focal length or the pixel size.

However, a competing factor that can mitigate the necessity for correction is the angular accuracy $d\varphi$ of the system and the detection process. This accuracy, in turn, is influenced by factors like the focal length and the pixel size, i.e., the pixel scale, alongside other contributing factors.

3. EXPERIMENTAL PROCEDURE FOR SENSOR CALIBRATION

The pixel delay arrays (start and stop array) vary for each camera/shutter combination. Additional factors such as fabrication inequalities can contribute to different delay times even within the same camera model. For a first estimation, the shape of the delay array can be approximated based on the shutter type and its provided temporal characteristics obtained from its data sheet.

For instance, a rolling shutter typically results in a linearly increasing delay time along one image axis, while a mechanical blade shutter creates an open delay array, with the smallest values located in the center of the image and progressively increasing towards the edges in a circular fashion.

For more precise delay information, it is necessary to conduct tests on both the shutter and the camera, recording their specific behaviors. The subsequent section outlines an experimental implementation of the method used to determine the delay array of a camera.

Figure 3 shows a schematic setup of a setup needed to measure the delay arrays of a camera.

This experimental setup includes:

- A camera with an output that indicates when the exposure starts or stops (FLI PL16803).

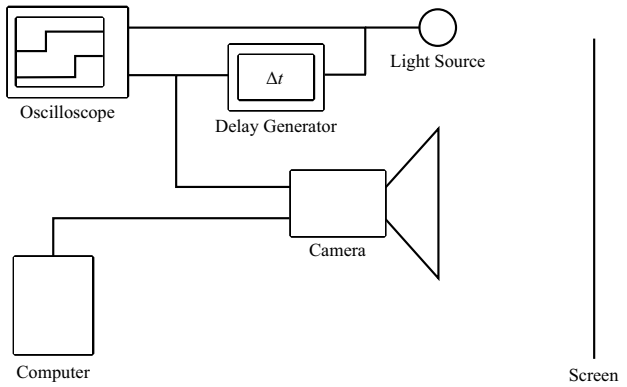

Fig. 3. Experimental setup for obtaining the delay array of a camera using a screen illumination method. The fast-switching light source is controlled by a delay generator, which triggers it after a time delay Δt following the camera's trigger signal.

- A fast-switching light source capable of being toggled on and off.
- A delay generator that can be triggered by the camera and switches the light source (e.g., a signal generator) (Agilent 33220A).
- A computer to control the camera and record the images.
- (Optional) An oscilloscope to verify the timing of the camera and the delay generator (Tektronix TDS 3034).

In the following, we'll first explain the measurement of the opening array of the camera/shutter combination. For this measurement, the light-emitting diode (LED) is initially turned on. The computer sends a command to the camera to request the recording of an image (at time t_0 in Fig. 4). After some time, the camera will start recording the image, and the shutter will start to open. Thus, the first pixels of the camera will be illuminated by the LED at time t_1. During the start of the image acquisition, the camera will also emit a trigger signal (at t_2). This is the signal that is typically detected with a GPS timer and is used as the "starting time" for passive optical measurements.

In our setup, the trigger output t_2 is fed into a delay generator, which adds a variable time delay Δt to generate a time t_3,

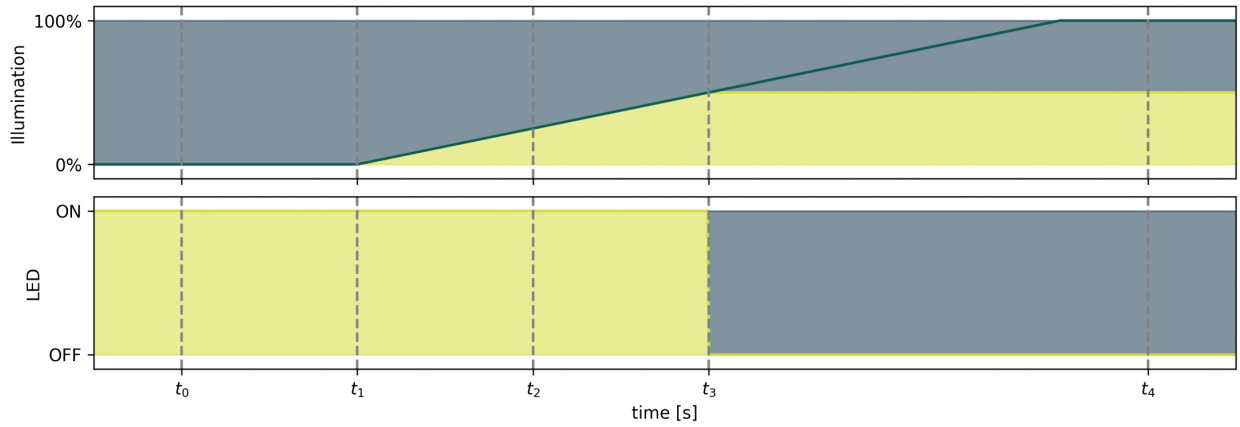

Fig. 4. Timing diagram illustrating the camera, LED, and trigger signal. The top plot displays the total illuminated area of the shutter, while the bottom plot indicates the LED state. The illuminated area increases after the shutter uncovers the first pixels at t_1 and stops to increase after the LED is switched off at t_3. The total uncovered area by the shutter is depicted with the solid line, which continues to increase even after the LED is switched off.

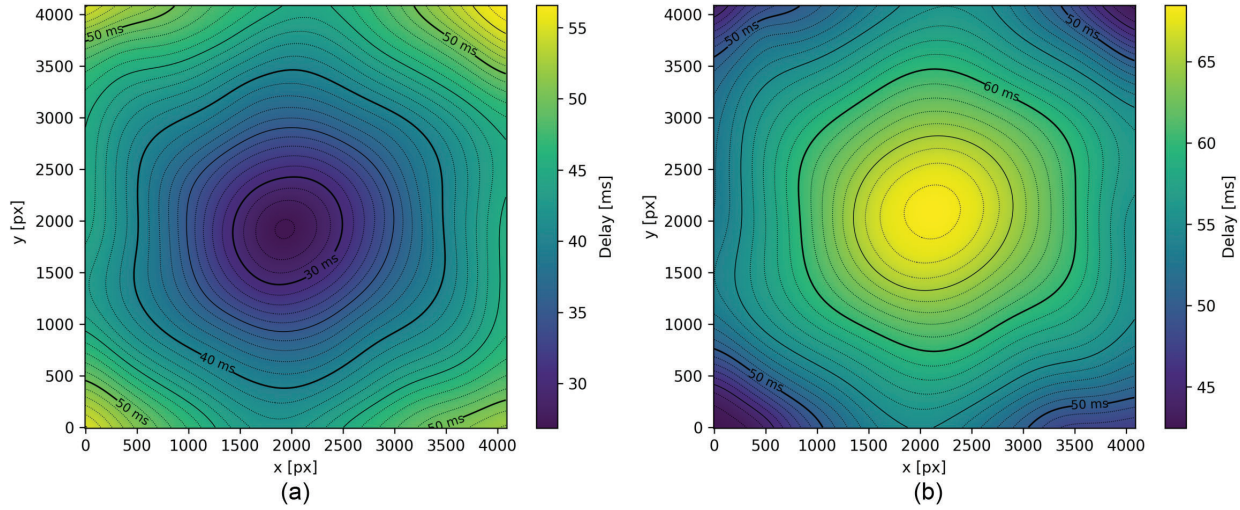

Fig. 5. Recorded delay arrays for the opening and closing time of the mechanical shutter used with the FLI PL16803 camera. (a) Opening delay array. (b) Closing delay array.

$$t_3 = t_2 + \Delta t; \quad \Delta t \in \mathbb{R}, \tag{13}$$

at which the light source is switched off.

Although the shutter continues to open after t_3, pixels uncovered afterwards are not illuminated anymore. The procedure is illustrated in the top plot of Fig. 4, where pixels registering light from the LED are displayed brightly.

Once the exposure time is reached, the camera stops the exposure, and the image is saved on the computer. The resulting image exhibits two sections, one bright, one dark. The border between the dark and the bright region indicates the position of the shutter at the delay time Δt after the trigger signal. To obtain a complete delay array, the measurement is repeated for different delay times Δt to ensure good coverage over the complete opening and closing times. The delay times Δt for all sensor pixels are combined in an array of the same size as the camera sensor. Any remaining gaps in the array are filled by interpolation. Since Δt is the difference between the actual exposure of a specific pixel and the time t_2 (as acquired with the GPS timer with passive optical sensors), it can be used as dt in Eq. (11) to correct the timing of the acquired data.

An analogous measurement procedure can be used to obtain the closing delay array. In this case, the LED is turned off in the beginning, and it is switched on at Δt after the exposure stop nobreaksignal.

Figure 5 shows experimental results for the camera (FLI PL16803 [24]) and a blade shutter. This camera/shutter combination was used in the evaluation campaign (see Section 4).

As anticipated, the delay arrays exhibit an increase/decrease from the center towards the edges of the image for the opening and closing of the shutter, respectively. Notably, at delay times corresponding to partial shutter openings, the shape of the shutter (which has six blades) becomes visible. Furthermore, the arrays show a slight asymmetry, which might be attributed to gravitational forces acting on the shutter. Fortunately, this effect is rather small, indicating that the delay arrays can be used independently of the orientation of the sensor during data acquisition.

4. EVALUATION

The proposed method was evaluated using experimental data from an observation campaign spanning from 2023-05-31 to 2023-06-22. The system utilized, known as APPARILLO, has been described previously [17] and includes a wide-angle staring camera designed to automatically detect sunlit space objects during nighttime under good weather conditions. The camera model, FLI PL16803 [24] is used with a Canon EF 135 mm f/2 lens, resulting in a total field of view of $\sim 15.7° \times 15.7°$ and a pixel scale of about 13.65 arcsec per pixel. Throughout the entire campaign, a binning of 2×2 pixels was employed to reduce the amount of stored data by approximately a factor of 4, leading to an effective resolution of around 27.3 arcsec.

Initially, the opening and closing delay arrays of the camera were measured as outlined in Section 3. Throughout the entire campaign, the camera was directed to an altitude angle of 45° with an azimuth of 0° at the location of the DLR premises in Stuttgart (48.7489°, 9.1026°, 538.0 m). During this period, 15 out of 23 nights had clear skies, in which the camera captured 27,892 images (approximately 2.3 TB of data) containing 16,016 recorded detections.

For further analysis, the streaks are cross-referenced with known satellites for which precise data are available. The TLE catalog obtained from the Space-Track website [25] is utilized to identify the specific satellite corresponding to each streak. However, for error analysis, TLE data alone is not precise enough, necessitating the use of high-precision laser ranging data (CPF data) obtained from the ftp server of the Technical University of Munich [26]. Due to limitations in data availability, this evaluation is restricted to 10 detections (from seven different satellites) over the entire observation campaign.

The CPF data serves as a prediction format, with prediction quality influenced by factors such as the number of target observations and the accuracy of orbit modeling [27]. Most of the remaining error in this prediction contributes to the along track direction and therefore to the time error. To mitigate prediction error in the analysis, CPF data with the closest epoch to the observation is selected, although some error may persist.

In high-precision applications like laser ranging, this error is addressed by third-party providers [28] publishing time biases for individual CPF data. Typically, these values are on the order of a few milliseconds, but in certain edge cases, they may increase. For the purposes of the following analysis, however, this difference will be disregarded.

By correlating the CPF data (which has a negligible error for this analysis) with the satellite streaks, the accuracy of each detection point can be assessed by comparing their positions at the time of observation.

To facilitate comparability between CPF data and detected data, a common coordinate system is necessary. Due to the absence of range information in passive optical detections, the CPF data are converted to the equatorial coordinate system using the skyfield Python package [29]. For this transformation, data points in the CPF data are interpolated to the time of detection using a 10-point Lagrange polynomial, as recommended in the Consolidated Laser Ranging Prediction Format Version 2.00 [30].

To derive the along and cross track errors, a velocity vector is needed, as explained in Eq. (5). This vector is obtained by introducing a small time increment, $dt = 1$ ms, to the detection time and calculating the position $\boldsymbol{r}(t + dt)$ at this adjusted time based on the CPF data. Subsequently, the shifted vector is also transformed to the equatorial coordinate system.

Given the satellite's movement along a straight line within a short time frame, and since the actual distance of the optical detection is unknown, all three vectors (the detection, the prediction, and the shifted prediction) are projected onto a sphere with a diameter of the range to the satellite determined from the CPF data. The conversion to a Cartesian coordinate system then enables the calculation of the along and cross track axes, as per Eq. (5). These axes are then directly used to calculate the along and cross track errors from the disparity between the detection and the prediction.

Before applying the proposed time correction method, the data were subjected to a precise astrometric calibration. Initially, the radial coordinates of the detected streaks were evaluated using the open-source astrometric calibration software astrometry.net [31]. This astrometric analysis was subsequently refined using data acquired from the GAIA star catalog [32,33] to get a better correction for image aberrations induced by the lens. Details of this refinement are provided in Appendix A.

After applying the corrected astrometry, the initially proposed time correction algorithm is implemented. As an example, Fig. 6 shows the along track error (each point corresponds to the end or starting point of a streak) during the overpass of the JASON 3 satellite at 2023-06-11 01:00:30 with and without using the time correction method. Note that there is a significant reduction in the along track error (from approximately 49 to 12 arcsec on average) when comparing the data before the time correction (blue triangles) to the data after the time correction (yellow triangles). This improvement is clearly seen for the data points corresponding to the starting points of each streak (when the shutter opens) as well as to the endpoints of the streaks (where the shutter closes). Note that the cross track error remains nearly unchanged by the time correction and is thus not plotted, but it can be found in Table 1. Thus, the ratio η between the along track and cross track errors decreases from 2.4 to 0.6 due to the timing correction.

For a more systematic evaluation, Fig. 7 shows the along track and cross track errors (with and without timing correction) for all detections from the measurement campaign, where precise CPF data were available. The underlying data and the reference to the specific satellite/measurement are provided in Table 1 (see Appendix B). In Fig. 7, the errors without timing correction (but with refined astrometry) are shown as blue squares. The standard deviation (scattering for different starting and ending points in the streaks) is depicted with the connected error bars. While the average along track error is only $\sim -9(16)$ arcsec, the along track error stands at $\sim 85(42)$ arcsec. The number in parentheses is the value of the uncertainty referring to the corresponding last digits of the result.

After applying the time correction, the average cross track error is almost unchanged $\sim -9(16)$ arcsec, but significantly reduces to $\sim 22(24)$ arcsec in the along track direction. As mentioned previously, a pure time correction does not significantly improve the residuals in the cross track direction, as the satellite

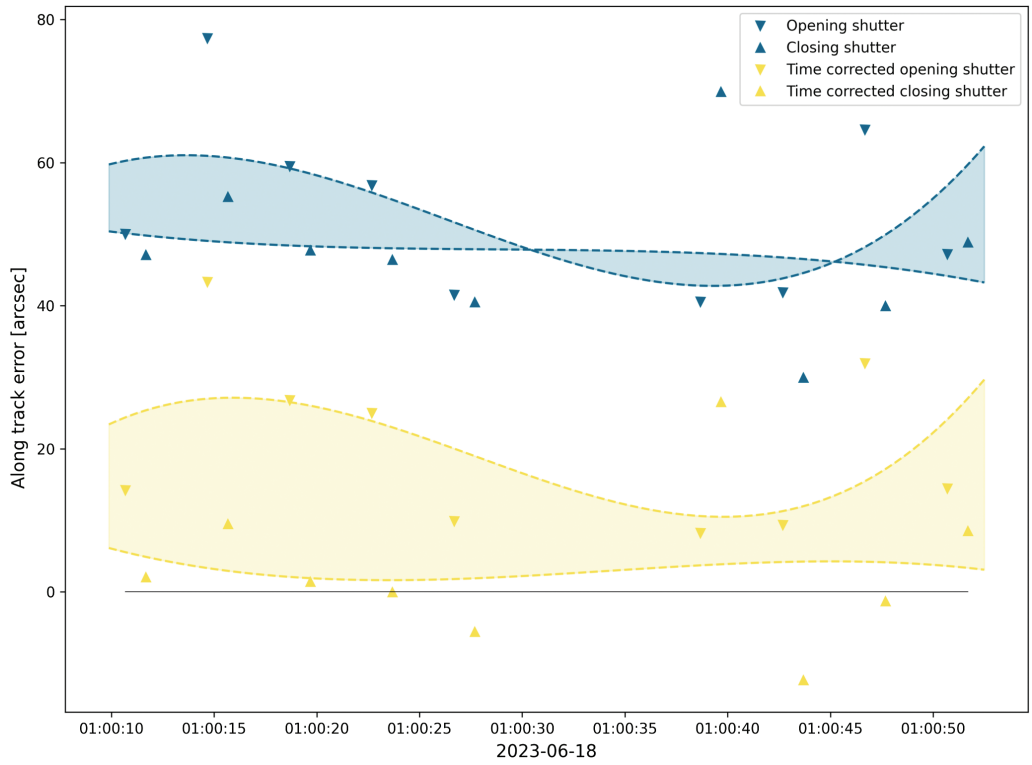

Fig. 6. Along track residuals of astrometric refined detections compared to the afterwards time-corrected detections of JASON 3 with respect to its CPF data obtained from [26]. The error in both cases is categorized into the opening and closing shutter phases.

Table 1. Performance of Time Correction Compared to Original Data Regarding Along-Track Δa and Cross-Track Δc Errors[a]

	Uncorrected			(Pure) Time Corrected			Astrometry Corrected			Both Corrections		
Satellite	Δc ["]	Δa ["]	η	Δc ["]	Δa ["]	η	Δc ["]	Δa ["]	η	Δc ["]	Δa ["]	η
HAIYANG 2C	−13(9)	66(29)	5.0	−13(9)	13(33)	1.0	−12(5)	64(25)	5.5	−12(5)	11(30)	1.0
HAIYANG 2D	4(9)	47(15)	12.5	4(9)	−4(18)	1.2	2(6)	47(13)	19.6	2(6)	−4(17)	1.7
JASON 3	11(5)	49(11)	4.4	11(5)	10(14)	0.9	21(3)	50(11)	2.4	21(3)	12(14)	0.6
HAIYANG 2D	−9(10)	43(44)	5.0	−9(10)	−9(47)	1.1	1(6)	42(39)	35.9	1(6)	−11(44)	9.2
SWARM A	−37(17)	138(48)	3.7	−37(17)	48(50)	1.3	−20(17)	132(41)	6.7	−20(17)	41(47)	2.1
SWARM C	−22(4)	141(36)	6.4	−22(4)	52(22)	2.3	−17(3)	145(30)	8.4	−17(3)	56(16)	3.3
HAIYANG 2D	−8(4)	65(32)	7.7	−8(4)	12(36)	1.4	−9(5)	62(24)	6.8	−9(5)	9(30)	1.0
SWARM C	−61(3)	113(51)	1.9	−61(3)	34(54)	0.6	−41(7)	110(53)	2.7	−41(7)	31(56)	0.7
SWARM A	−15(3)	145(38)	9.5	−15(3)	58(29)	3.8	−20(4)	151(33)	7.4	−20(4)	63(26)	3.1
SENTINEL 6	−18(6)	43(15)	2.5	−18(6)	4(18)	0.2	4(3)	49(17)	13.5	4(3)	10(19)	2.8
Mean	**−17(7)**	**85(42)**	**5.9**	**−17(19)**	**22(23)**	**1.4**	**−9(16)**	**85(42)**	**10.9**	**−9(16)**	**22(24)**	**2.5**

[a]The ratio η represents the mean value of Δa divided by Δc for each satellite. Standard deviations for individual overpasses are shown in parentheses, while this value for the "Mean" row denotes the standard deviation of the individual η values.

primarily moves along the track direction. This is evident in the plot, where all time-corrected residuals, indicated by yellow triangles and error bars, only shift along the y-axis. Both along track and cross track errors scatter around the zero point after correction, within one pixel resolution as indicated by dashed lines. Apart from reducing the absolute values, the method also decreases the standard deviation of the scattered mean values, thus increasing the precision.

5. CONCLUSION AND OUTLOOK

The proposed method leverages individual timing differences in cameras lacking a global shutter to enhance the overall accuracy and precision of detected space objects. It involves incorporating pixel-dependent time corrections into the global timestamp of detected sources in the image and is adaptable to cameras with any shutter type.

In our validation campaign, the along track error reduces by 74% to approximately 22 arcsec. Moreover, the ratio of along track to cross track error decreases by 77% to a value of 2.5, with the cross track error post-correction measuring approximately −9 arcsec, resulting in comparable accuracy in both directions.

A noteworthy accomplishment of this study is the reduction of both errors to values below the pixel resolution (27.3 arcsec) of the camera, as streak detection relies on this quantized pixel information. To further diminish the along track error, it might

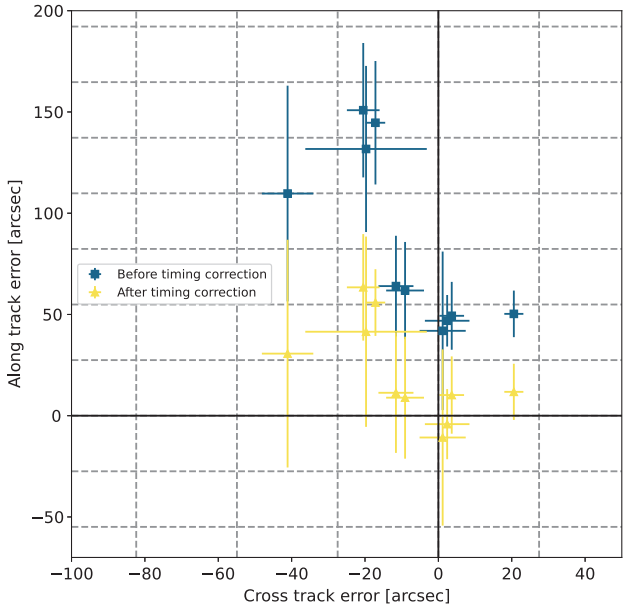

Fig. 7. Comparison of the residuals obtained from all detections throughout the complete observation campaign spanning from 2023-05-31 to 2023-06-22. The plot illustrates residuals from the refined astrometric calibration (blue squares) and from the afterwards time-corrected detections (yellow triangles). In the latter case, the correction notably enhances most residuals below the limit of the pixel resolution, indicated by the dashed lines.

be possible to further refine the detection of streak start and endpoints, which likely constitute the primary small source of remaining error.

The proposed method has so far only been tested with an Earth based staring sensor pointing to a fixed direction in space. The method can however similarly be used for tracking sensors or space based (staring) sensors. In case of a tracking sensor, it has to be considered that the starting and endpoints of the streaks (in that case coming from the stars) are actually recorded at slightly different times. Thus, a precise astrometric calibration requires an extrapolation of these points to a common time, and we hope to demonstrate this in future work.

Furthermore, the described timing correction has so far only been done in post-processing of the data. Currently, the authors are working on fully automated data processing that will generate precise CPF files (including the timing correction) within seconds after the image acquisition with the staring sensor.

APPENDIX A: EXPERIMENTAL DETAILS FOR THE IMPROVED ASTROMETRIC ANALYSIS

During the testing of the new time correction method, the accuracy of the used astrometric calibration shifted into focus. It became clear that the detected stars (yellow crosses in Fig. 9) diverge from the same stars listed in the GAIA catalog [32,33] projected into the image with the obtained astrometric calibration.

This discrepancy is more pronounced at the edges of the image (see Fig. 9) and reaches values ∼2 px, which corresponds to 55 arcsec with the camera configuration.

The applied refined astrometric calibration is based on the current one, and the detected star differences are used to improve the induced error especially in the extreme areas.

The collected data are autonomously recorded and processed, including the conversion of the pixel coordinates of the streaks to equatorial coordinates. This conversion is facilitated by the astrometric calibration software astrometry.net [31], because of its reliability in generating "wcs-files" used for coordinate transformation, with a measured elapsed time of approximately 0.5 s to enable real-time processing of each image.

To achieve such fast processing times, a coarse estimate of the position, the image dimensions, and the selection of a subset of 20 stars is necessary. However, this approach limits the software's ability to compensate for lens distortions or slightly miss-detected star centers. Increasing the number of stars significantly extends the astrometric calibration time.

For the improved method, all stars with a magnitude lower than 12 within the field of view are queried from the GAIA catalog [32,33]. The magnitude threshold is selected based on the camera system's capability to record these magnitudes with a sufficient signal-to-noise ratio for detection by the star detection algorithm.

The selected catalog stars are then transformed into the pixel coordinate system using the wcs-file obtained from astrometry.net. Subsequently, the two categories, catalog stars and detected stars, are correlated using a KDTree algorithm. Pairs of stars with a distance greater than 5 pixels are discarded, as they are likely not a real match. The astrometric calibration is then corrected based on the difference of the remaining pairs.

To interpolate the correction to the actual position of the detected streak, a B-spline interpolation over the complete image is used. This interpolation technique additionally compensates for single miss-detected stars by using multiple stars in the vicinity. It has the benefit compared to a pure polynomial interpolation that at the edges of the image the interpolation is not drastically over-compensating the correction. A different interpolation that only uses neighboring stars and interpolates between them would lead to a wrong correction, if stars are miss-detected. Both alternatives yield in an overall worse performance.

A histogram illustrating their differences before correction is depicted in Fig. 8. The distribution's mean position at $(x: 0.8 | y: -0.2)$ suggests that the standard astrometric calibration exhibits some bias, while the standard deviation measures at $(dx: 1.45 | dy: 0.6)$. This bias arises from the inherent limitation of the astrometric calibration with a limited number of 20 stars.

In addition to the histogram, Fig. 8, the differences between the corrected stars and the stars predicted by the GAIA catalogue are displayed. The mean position is reduced to $(x: 0 | y: 0)$, with a corresponding reduction in standard deviation to $(dx: 0.6 | dy: 0.5)$. Notably, significant differences are observed, especially at the edges of the image, leading to a more Gaussian-shaped distribution and a reduction in outliers. The impact on star detection within an image is depicted in Fig. 9. Here, the center of the detected star is marked in yellow, while the predicted position by the astrometric calibration is marked in blue. In the complete image shown on the left side; individual differences may not be visible, but an increase of

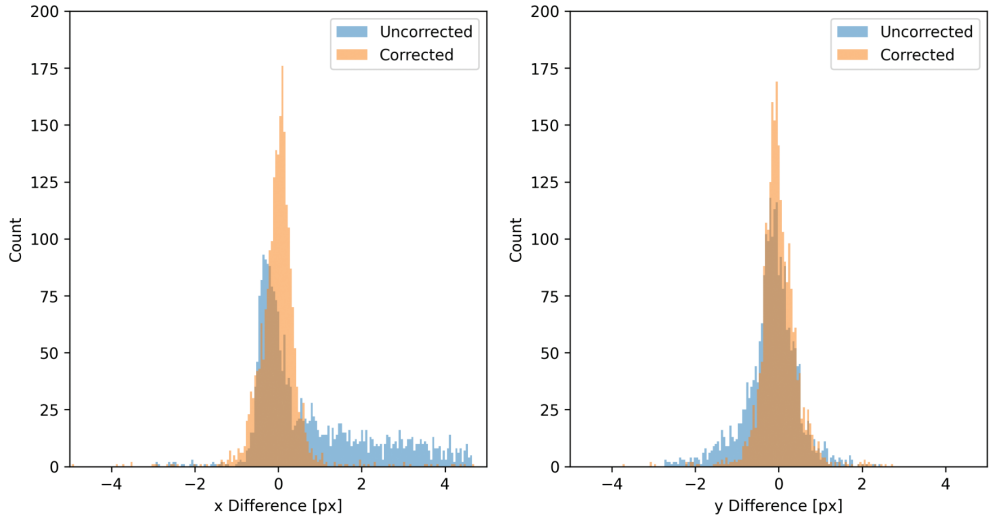

Fig. 8. Histogram displaying the differences between detected stars and stars predicted by the astrometric calibration using the GAIA catalog before and after the astrometric correction. The difference is separated into the x and y direction, and the correction primarily targets outliers, resulting in a distribution that aligns more closely with a Gaussian distribution.

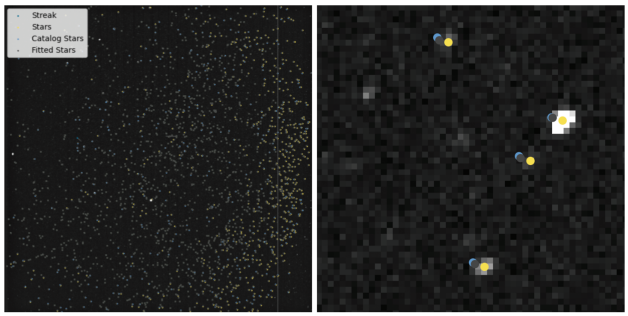

Fig. 9. Comparison of detected star positions (blue) and positions predicted by the astrometric calibration using the GAIA catalog, before (yellow) and after (gray) astrometric correction. In image (a), discrepancies are more pronounced at the image edges, indicated by yellowish color. Image (b) zooms in on a section of the left image, highlighting differences. (a) Complete image. (b) Zoomed in section.

yellowish tones towards the left suggests that the catalog stars, marked in blue, do not align with those of the detected stars in this area.

On the right side, a zoomed-in version of the left image section is presented. To correct a coordinate in the image, whether a star or a streak, the value of the fitted B-spline at that position is subtracted from the original value. Corrected stars are indicated by gray crosses in Fig. 9. For completeness, the result is transformed back into equatorial coordinates using the original wcs-file.

Further refinement of the pixel-to-equatorial coordinates transformation, with an atmospheric correction, is not necessary due to the limited pixel scale of 27.3 arcsec and the close proximity of reference stars to each streak.

APPENDIX B: DATA FOR THE ACCURACY OF DETECTED STREAKS FOR SATELLITES WITH AVAILABLE CPF DATA

Detailed information about the accuracy of the measurement and the impact of the two proposed correction methods is displayed in Table 1.

Acknowledgment. The authors acknowledge DLR internal funding from the Technology Transfer. Furthermore, helpful discussions with Dr. Hauke Fiedler and colleagues (DLR German Space Operations Center) are greatly acknowledged.

Disclosures. The authors declare no conflicts of interest.

Data availability. Additional data (TDM, delay arrays, FITS, etc.) that support the findings of this study are available from the corresponding author upon reasonable request.

REFERENCES

1. D. L. Oltrogge, "The 'we' approach to space traffic management," *SpaceOps Conference*, Marseille, France, 28 May–1 June, 2018.
2. ESA Space Debris Office, "ESA's annual space environment report," Tech. rep. (ESA, 2023).
3. C. Manfletti, M. Guimarães, and C. Soares, "AI for space traffic management," J. Space Saf. Eng. **10**, 495–504 (2023).
4. Bundesministerium für Wirtschaft und Klimaschutz (BMWK), *Raumfahrtstrategie der Bundesregierung* (BMWK, 2023).
5. G. Fonder, M. Hughes, M. Dickson, *et al.*, "Space fence radar overview," *International Applied Computational Electromagnetics Society Symposium (ACES)*, Miami, Florida, 2019.
6. J. Rowland, D. McKnight, B. P. Pino, *et al.*, "A worldwide network of radars for space domain awareness in low earth orbit," in *Advanced Maui Optical and Space Surveillance Technologies Conference (AMOS)* (2021).
7. H. Yunpeng, L. Kebo, L. Yan'gang, *et al.*, "Review on strategies of space-based optical space situational awareness," J. Syst. Eng. Electron. **32**, 1152–1166 (2021).
8. H. Fiedler, J. Herzog, M. Prohaska, *et al.*, "Smartnet-an update," in *ESA NEO and Debris Detection Conference* (2019).
9. E. Cordelli, A. Vananti, and T. Schildknecht, "Analysis of laser ranges and angular measurements data fusion for space debris orbit determination," Adv. Space Res. **65**, 419–434 (2020).

10. D. Hampf, W. Riede, N. Bartels, *et al.*, "A path towards low-cost, high-accuracy orbital object monitoring," in *Proceedings 8th European Conference on Space Debris* (2021).
11. M. Vasile, L. Walker, A. Campbell, *et al.*, "Space object identification and classification from hyperspectral material analysis," Sci. Rep. **14**, 1570 (2024).
12. M. Nussbaum, E. Schafer, Z. Yoon, *et al.*, "Spectral light curve simulation for parameter estimation from space debris," Aerospace **9**, 403 (2022).
13. A. Rachman, T. Schildknecht, and A. Vananti, "Analysis of temporal evolution of debris objects' rotation rates inside AIUB light curve database," in *69th International Astronautical Congress* (2018).
14. Z. Wang, X. Ji, J.-B. Huang, *et al.*, "Neural global shutter: Learn to restore video from a rolling shutter camera with global reset feature," in *IEEE/CVF Conference on Computer Vision and Pattern Recognition (CVPR)* (2022), pp. 17773–17782.
15. A. Gurgul, M. Drzał, A. Sybilska, *et al.*, "LightStream–enhancements to the Astrometry24.NET software for processing SST and asteroid images from CCD and CMOS," in *2nd NEO and Debris Detection Conference* (2023), p. 76.
16. J. B. J. Shaddix, A. H. A. Ferris, and T. M. A. Larson, "Daytime geo tracking with 'aquila': Approach and results from a new ground-based swir small telescope system," in *Advanced Maui Optical and Space Surveillance Technologies Conference (AMOS)* (2019).
17. P. Wagner and T. Clausen, "Apparillo: a fully operational and autonomous staring system for leo debris detection," CEAS Space J. **14**, 303–326 (2021).
18. T. C. C. for Space Data Systems (CCSDS), "Tracking data message," CCSD Standard 503.0-B-2 (2020).
19. V. Associates, "Uniblitz cs65, 65 mm uni-stable optical shutter, version 6.0," (2022).
20. Finger Lake Instruments, "Kepler manual, rolling shutter overview," (2018).
21. A. Vananti, K. Schild, and T. Schildknecht, "Improved detection of faint streaks based on a streak-like spatial filter," Adv. Space Res. **65**, 364–378 (2020).
22. P. Zimmer, M. Ackermann, and J. McGraw, "GPU-accelerated faint streak detection for uncued surveillance of LEO," in *Advanced Maui Optical and Space Surveillance Technologies Conference (AMOS)* (2013).
23. R. Haussmann, P. Wagner, and T. Clausen, "Streak detection of space debris by a passive optical sensor," in *8th European Conference on Space Debris* (2021).
24. Finger Lake Instruments, "Proline PL16803."
25. Space-Track, "Full catalog 3LE."
26. Technische Universität München, "Eurolas data center," 2023, https://edc.dgfi.tum.de/en/.
27. S. Bauer and J. Steinborn, "Time bias service: analysis and monitoring of satellite orbit prediction quality," J. Geod. **93**, 2367–2377 (2019).
28. S. Bauer and J. Steinborn, "CPF time bias prediction," 2024, http://slr.gfz-potsdam.de:5000/tb/v1.
29. B. Rhodes, "Skyfield: high precision research-grade positions for planets and Earth satellites generator," Astrophysics Source Code Library, record ascl:1907.024 (2019).
30. ILRS, "Consolidated laser ranging prediction format, version 2.00," (2018).
31. D. Lang, D. W. Hogg, K. Mierle, *et al.*, "Astrometry.net: Blind astrometric calibration of arbitrary astronomical images," Astron. J. **139**, 1782 (2010).
32. Gaia Collaboration, T. Prusti and J. de Bruijne, "The GAIA mission," Astron. Astrophys. **595**, A1 (2016).
33. Gaia Collaboration, A. Vallenari and A. G. A. Brown, "Gaia early data release 3: Summary of the contents and survey properties (corrigendum)," Astron. Astrophys. **650**, C3 (2021).

323 247 247 248]/s /2024-06-21 14:45:12]